Scientific Reports
https://doi.org/10.1038/s41598-026-37357-6

Article in Press

Determination of mechanical properties of ceramic microspheres using an improved flat-plate crushing test and global cohesive zone modeling

Received: 24 September 2025

Accepted: 21 January 2026

Published online: 24 January 2026

Cite this article as: Ma H., Lv J., Zhou Y. *et al.* Determination of mechanical properties of ceramic microspheres using an improved flat-plate crushing test and global cohesive zone modeling. *Sci Rep* (2026). https://doi.org/10.1038/s41598-026-37357-6

Haojun Ma, Junnan Lv, Yubo Zhou, Yingxuan Dong, Yingzheng Song & Qun Li

We are providing an unedited version of this manuscript to give early access to its findings. Before final publication, the manuscript will undergo further editing. Please note there may be errors present which affect the content, and all legal disclaimers apply.

If this paper is publishing under a Transparent Peer Review model then Peer Review reports will publish with the final article.

ARTICLE IN PRESS

© The Author(s) 2026. **Open Access** This article is licensed under a Creative Commons Attribution-NonCommercial-NoDerivatives 4.0 International License, which permits any non-commercial use, sharing, distribution and reproduction in any medium or format, as long as you give appropriate credit to the original author(s) and the source, provide a link to the Creative Commons licence, and indicate if you modified the licensed material. You do not have permission under this licence to share adapted material derived from this article or parts of it. The images or other third party material in this article are included in the article's Creative Commons licence, unless indicated otherwise in a credit line to the material. If material is not included in the article's Creative Commons licence and your intended use is not permitted by statutory regulation or exceeds the permitted use, you will need to obtain permission directly from the copyright holder. To view a copy of this licence, visit http://creativecommons.org/licenses/by-nc-nd/4.0/.

Determination of Mechanical Properties of Ceramic Microspheres Using an Improved Flat-Plate Crushing Test and Global Cohesive Zone Modeling

Haojun Ma[a], Junnan Lv[c,*] , Yubo Zhou[a], Yingxuan Dong [a,b], Yingzheng Song[a], Qun Li [a,*]

Email Address of the Corresponding Author: **junnanlv@foxmail.com**

[a]State Key Laboratory for Strength and Vibration of Mechanical Structures, School of Aerospace, Xi’an Jiaotong University, Xi’an 710049, China

[b]Department of Civil and Environmental Engineering, National University of Singapore, Singapore 119260, Singapore

[c]National Key Laboratory of Nuclear Reactor Technology, Nuclear Power Institute of China, Chengdu 610213, China

Abstract：

Ceramic microspheres are widely used in various applications, such as nuclear fuel particles in reactors, ZrO_2 particles for bone fillers, and SiC particles for precision grinding media. To improve the mechanical performance and enhance the safety of these microspheres, the ability to rapidly and accurately determine their mechanical properties is of critical importance. However, due to the close relationship between the fabrication process, microstructure, and internal defect configuration of ceramic microspheres, their mechanical characterization cannot be effectively conducted using conventional methods that ignore the spherical geometry. At present, no standardized experimental technique or computational model exists for such evaluation. This study investigates the crushing mechanics of ceramic microspheres by combining an improved flat-plate crushing test with numerical simulations. Polycrystalline diamond (PCD) was adopted to enhance the conventional flat-plate crushing setup, which typically exhibits low sensitivity to specimen size but is not suitable for high-hardness materials. A dedicated high-precision experimental device was developed for testing sub-millimeter ceramic microspheres. Six groups of ZrO_2 microspheres with varying diameters were tested, yielding precise force–displacement curves that captured the complete crushing process. In parallel, numerical simulations based on Voronoi tessellation and global cohesive elements were conducted to replicate the crushing process. By calibrating the model to match the experimental force–displacement curves, the mechanical parameters of the microspheres were determined in a scientifically reliable and precise manner. This integrated approach provides a new perspective for evaluating the mechanical properties of ceramic microspheres.

Keywords

Ceramic microspheres; Flat-plate crushing test; Cohesive zone elements; Fracture simulation; Fracture toughness

1. Introduction

The safety of nuclear power facilities is of paramount importance worldwide, and it is directly dependent on the integrity of reactor fuel systems. During the out-of-pile fabrication stage of fuel elements, the assembled fuel compacts undergo multiple rolling processes. In these procedures, some fuel particles inevitably fracture due to insufficient strength and toughness, which can compromise the in-pile performance of the fuel elements. If the internal fracture rate of fuel particles is excessively high, numerous microcracks may nucleate and propagate through the matrix, eventually forming macroscopic cracks extending several millimeters in length. Such damage poses a serious threat to the safe operation of nuclear reactors. In fact, the fracture failure of fuel particles is considered the root cause of structural failure in dispersion-type fuel elements. Similarly, ceramic microspheres are widely used in medical and industrial applications, including bone grafting materials and catalyst supports. To further improve their fabrication processes and performance, it is essential to accurately determine their mechanical properties, particularly their fracture behavior, which remains a key challenge to be addressed.

Currently, the commonly used testing methods for ceramic spheres include the two-ball and three-ball compression tests (standards JB/T 1255 and JIS D9418-2001), bending tests (standards ASTM C1161 and GB/T 4741-1999), the three-ball-to-sphere test [1], the “C-sphere” method [2], and the notched-sphere method [3] derived from the improved “C-sphere” technique. Prior to fracture, the assembly is subjected to a monotonically increasing compressive load, and the peak load at failure is defined as the "fracture load." This method enables the evaluation of the material's strength, toughness, and elastic modulus. The bending strength test is currently the most widely adopted technique for characterizing the mechanical properties of ceramic materials and is governed by well-established standards. This method is also applicable to measuring the tensile and flexural strength of glass specimens and assessing fracture behavior [4]. Moreover, it has been used to characterize the mechanical models of quasi-brittle materials such as rocks and concrete [5].

The ball-on-three-ball (B3B) test has also emerged as one of the widely adopted methods for evaluating ceramic materials. In this configuration, a ceramic disc is supported by three balls on one side and loaded axially by a fourth ball from the opposite side. Compared to uniaxial testing, the B3B method offers easier specimen preparation, is suitable for thin disc-shaped samples, and, due to its biaxial loading nature, better reflects real-world engineering conditions. Additionally, it enables the testing of a large surface area free from edge finishing defects [1]. Based on linear axisymmetric thin plate theory, Bassali [6] derived the maximum tensile stress at the center of the disc, which was later refined by Kirstein [7]. However, the B3B test inherently involves a complex three-dimensional stress state, making it difficult to obtain exact analytical solutions. Therefore, finite element analysis is commonly employed to assist in the evaluation, and more recently, researchers have proposed new fitting functions for stress assessment in B3B testing [8].

Both flexural and B3B tests require specimens to be fabricated using identical manufacturing procedures, which are often costly and time-consuming. Furthermore, the measured strength in such tests typically corresponds to failure initiated by internal material damage. In contrast, compressive failure of ceramic spheres usually originates at surface regions experiencing high tensile stress, particularly at or near polished surfaces. As a result, the measured properties may not fully represent the mechanical behavior encountered in actual application scenarios.

To address the aforementioned issues, Wereszczak et al. [2] devised and developed a method involving the machining of a groove with a fixed depth on the surface of the ceramic sphere, transforming it into a "C-sphere." A simple and monotonic uniaxial compressive load is then applied to the C-sphere, inducing tensile stress on its outer surface and ultimately causing fracture. The strength is determined by integrating the failure load, the C-sphere geometry, and finite element analysis. This method features a very simple geometry and is easy to implement in testing. Similarly, Strobl et al. [3,9] proposed an in-situ testing method on ceramic spheres. After a detailed analysis using the finite element method, a narrow notch is introduced along the equatorial plane of the sphere. When a compressive load is applied perpendicular to the notch direction, tensile stress is induced on the surface region opposite the notch, leading to fracture failure.

It is evident that various experimental approaches have been developed for characterizing the mechanical properties of ceramic spheres across a wide range of sizes, and substantial progress has been made in this area. However, for many sub-millimeter ceramic microspheres—such as UO_2 or UN fuel particles used in nuclear reactors [10,11], and ZrO_2 particles used as bone fillers—with diameters typically ranging from 0.3 mm to 0.8 mm, current research remains limited. The inherent internal defect structures within ceramics lead to considerable variability in their mechanical properties, and the small size of microspheres may further intensify this dispersion. Consequently, testing methods that involve introducing artificial cracks or cutting notches on the sphere surface are extremely inefficient and make it difficult to accurately capture such variability. Therefore, it remains challenging to evaluate the mechanical properties of ceramic microspheres independently of their spherical geometry. As a result, the existing experimental techniques are inadequate for directly measuring the mechanical properties of ceramic microspheres, and no standardized testing protocol currently exists.

Similarly, researchers have attempted to compress spheres between two parallel flat platens until fracture occurs. This test primarily evaluates the resistance to cumulative damage and is therefore more related to the material’s toughness, plasticity, and Young’s modulus rather than its intrinsic strength [12]. The method is largely insensitive to specimen size and has been widely employed in the testing of rock [13] and gravel [14], making it well suited for the present study. However, significant stresses develop only in the contact regions between the sphere and the platens. Because these high-stress zones are in close proximity, the actual amplitude of the maximum tensile stress is highly sensitive to the characteristics of the contact area. Factors such as plastic deformation of the platens, friction at the sphere–platen interface, and surface roughness of the platens can all strongly influence the results [3]. These issues represent the key challenges to be addressed in flat-plate compression testing.

The crushing test enables a direct comparison of the fracture behavior of different ceramic spheres through their force–displacement curves; however, it cannot quantitatively determine their mechanical properties. Therefore, employing numerical simulations to indirectly obtain fracture mechanical parameters represents a highly effective approach. The cohesive zone model (CZM) is a numerical method based on continuum damage mechanics, in which a cohesive element is inserted between two solid elements to represent the traction–separation relationship at their interface. The softening behavior described by this relationship reflects the degradation of material stiffness due to damage evolution. This degradation capability allows the CZM to simulate progressive fracture processes. The implementation of the cohesive model requires cohesive elements to be pre-inserted along potential crack paths to capture the corresponding mechanical response.

CZM-based approaches have been extensively investigated. For example, Guo [15] and Hou [16] constructed interfacial bonding layers in composite materials using cohesive elements. The core of CZM lies in the well-defined traction–separation constitutive relationships. Various cohesive laws have been proposed over time, including the bilinear and exponential models by Xu and Needleman [17], the trapezoidal model by Tvergaard and Hutchinson [18,19], the trilinear model proposed by Donadon et al. [20], and the linear–parabolic model developed by Allix O [21,22]. Regardless of the specific form of the cohesive constitutive relationship, the cohesive energy represents the total work per unit area required to completely fail a cohesive element, which equals the fracture toughness G_c [23]. Among these, the bilinear model is widely adopted due to its simplicity and clear physical interpretation.

Therefore, this study aims to improve the flat-plate (flat-to-flat) compression testing method for sub-millimeter ceramic microspheres of various sizes, by eliminating the limitations of conventional tests and obtaining accurate force-displacement curves throughout the crushing process. A numerical simulation approach is adopted to model the crushing behavior of ceramic microspheres and to derive their mechanical properties. In Section 2, the flat crushing test setup is enhanced by replacing conventional metallic platens with customized platens made of PCD composites. This effectively resolves issues related to plastic deformation, insufficient hardness, and high surface roughness of traditional metal platens. The resulting configuration forms a contact between three elastic bodies, enabling the flat-plate crushing test to be applied to high-hardness, sub-millimeter ceramic microspheres. Considering the radiation hazards of uranium dioxide, zirconia microspheres—known for their higher strength, greater hardness, and wide range of applications—were selected for experimental validation. The customized experimental platform successfully produced accurate and reliable force-displacement curves, with comprehensive analysis of the results. In Section 3, a numerical model of the zirconia microsphere was constructed using Voronoi tessellation to introduce mesh randomness, and global cohesive zone elements were embedded to simulate the full crushing process. Finite element simulations were conducted to analyze the stress and strain distribution during crushing, and the use of both cohesive and bulk material parameters yielded elastic modulus and fracture toughness values consistent with those reported in the literature. Finally, Section 4 summarizes the key conclusions of this study.

2. Crushing Experiment

2.1. Materials and Methods

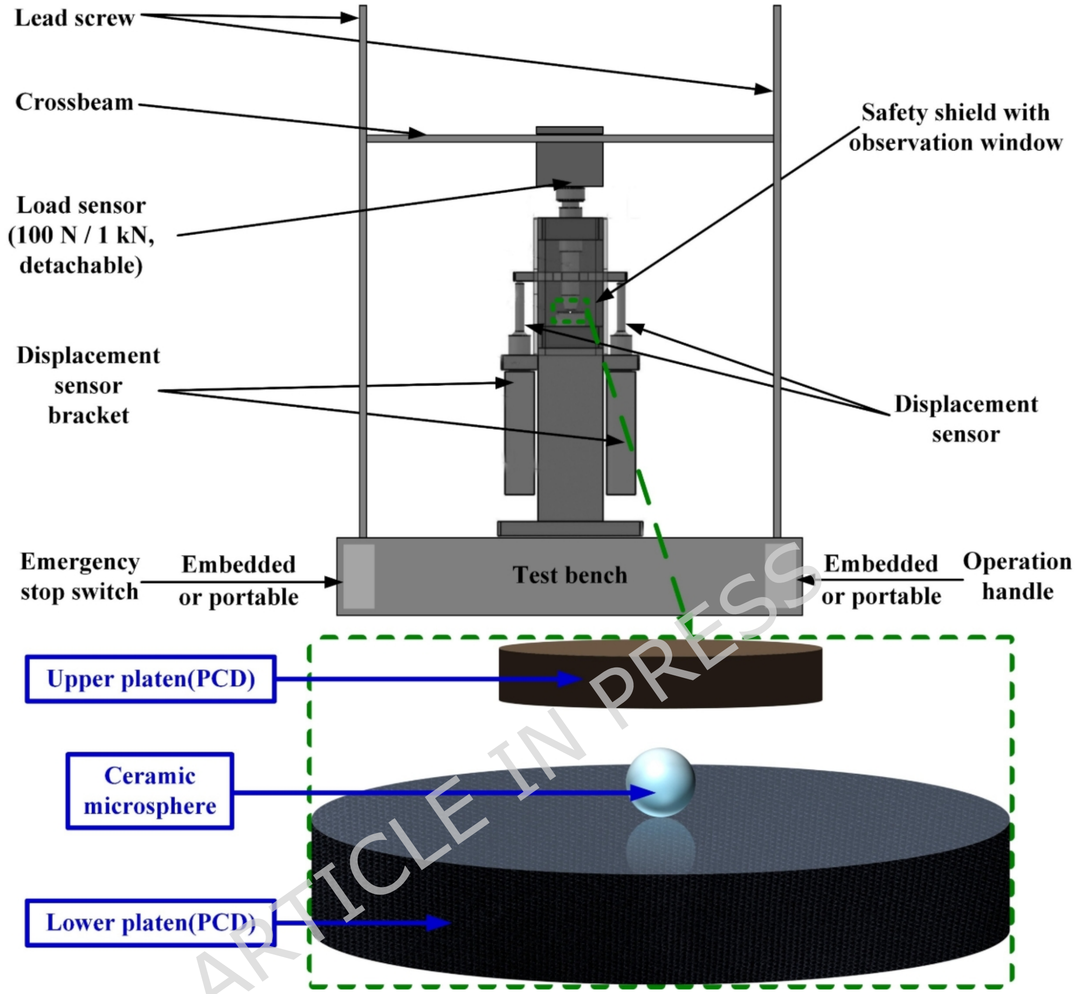

Fig. 1. Schematic diagram of the crush test.

This study developed a dedicated crushing test platform tailored to spherical particles with diameters smaller than one millimeter, employing a flat-plate compression configuration (hereafter referred to as the crushing test). A schematic of the setup is shown in Fig. 1. The ceramic microspheres investigated in this study are composed of extremely hard materials. To prevent equipment wear and ensure accurate measurements, diamond is the ideal material for both platens and compression heads. However, fabricating platens entirely from single-crystal diamond would be prohibitively expensive. As an alternative, this study employs PCD—a material commonly used in aerospace milling tools—as the platen material. PCD is a composite material produced by sintering diamond microparticles and a binder under ultrahigh pressure and high temperature. Its grains are randomly oriented, resulting in uniform hardness and isotropic mechanical behavior. This contributes to a very low coefficient of friction; according to published data, the friction coefficient between zirconia and PCD plates is only 0.12 [24]. Furthermore, being composed entirely of sintered diamond particles, PCD possesses a hardness far exceeding that of the ceramic microspheres under investigation.

The test specimens used in this study are zirconia ceramic microspheres sintered at 1450 °C with yttria as a sintering aid, specifically composed of 3 mol% yttria-stabilized tetragonal zirconia polycrystals (3Y-TZP). The fracture toughness K_{Ic} of the zirconia ceramics ranges from 5.2 to 8.1 $MPa{\cdot}\mathrm{m}^{0.5}$, while the remaining mechanical properties are summarized in Table 1 and were provided by the manufacturers. The material parameters supplied by the manufacturers are consistent with the results reported in existing literature [25-28]. The PCD composite platens were manufactured by Henan Huanghe Whirlwind Co., Ltd. The diamond layer thickness of the PCD composite platen was 0.5 mm. The working surface was polished to achieve a surface roughness below 0.05 μm, as determined by measuring the platen surface using a three-dimensional optical surface profilometer based on white-light interferometry and calculating the arithmetic average roughness (Ra). As a result, the platen surface exhibited a mirror-like finish. The precision zirconia microspheres were supplied by Pingxiang

Jinxiang New Materials Co., Ltd.

Table 1

Mechanical Properties of the Tested Material

Material	Hardness	Elastic Modulus (GPa)	Poisson’s Ratio
PCD	90GPa (HK_n)	919	0.09
ZrO_2	1400 (HV)	220±15	0.30

To facilitate the observation of deformation in the platens, a larger (9 mm) ZrO_2 ceramic ball was first tested using an 880/10T high–low temperature testing machine to verify whether the PCD composite plates could sustain high loads while undergoing only elastic deformation. Upon successful validation, a customized testing platform was constructed, employing a benchtop dual-column frame equipped with a precision ball screw and dual guide rods. The loading system is controlled by a high-precision actuator, with a speed control error of less than ±0.5% of the set value. The load sensors used in this apparatus were supplied by Hamk-Tech Corporation, comprising two high-precision units: one with a maximum capacity of 100 N and the other 1000 N, both featuring automatic zeroing and self-calibration. The load measurement accuracy is within ±3% of the reading when the load is between 0.05% and 0.1% of full capacity, within ±2% when between 0.1% and 1%, and within ±1% when between 1% and 100%. The data acquisition rate exceeds 5000 Hz. The displacement sensor was provided by Mitutoyo Corporation and employs a high-precision photoelectric linear gauge, with a gauge length range of 0–10 mm, a resolution of 0.1 μm, and a measurement accuracy within ±2% of the reading. This setup ensures the precise measurement of force–displacement curves for sub-millimeter ceramic microspheres. The detailed configuration of the experimental apparatus is shown in Fig. 2.

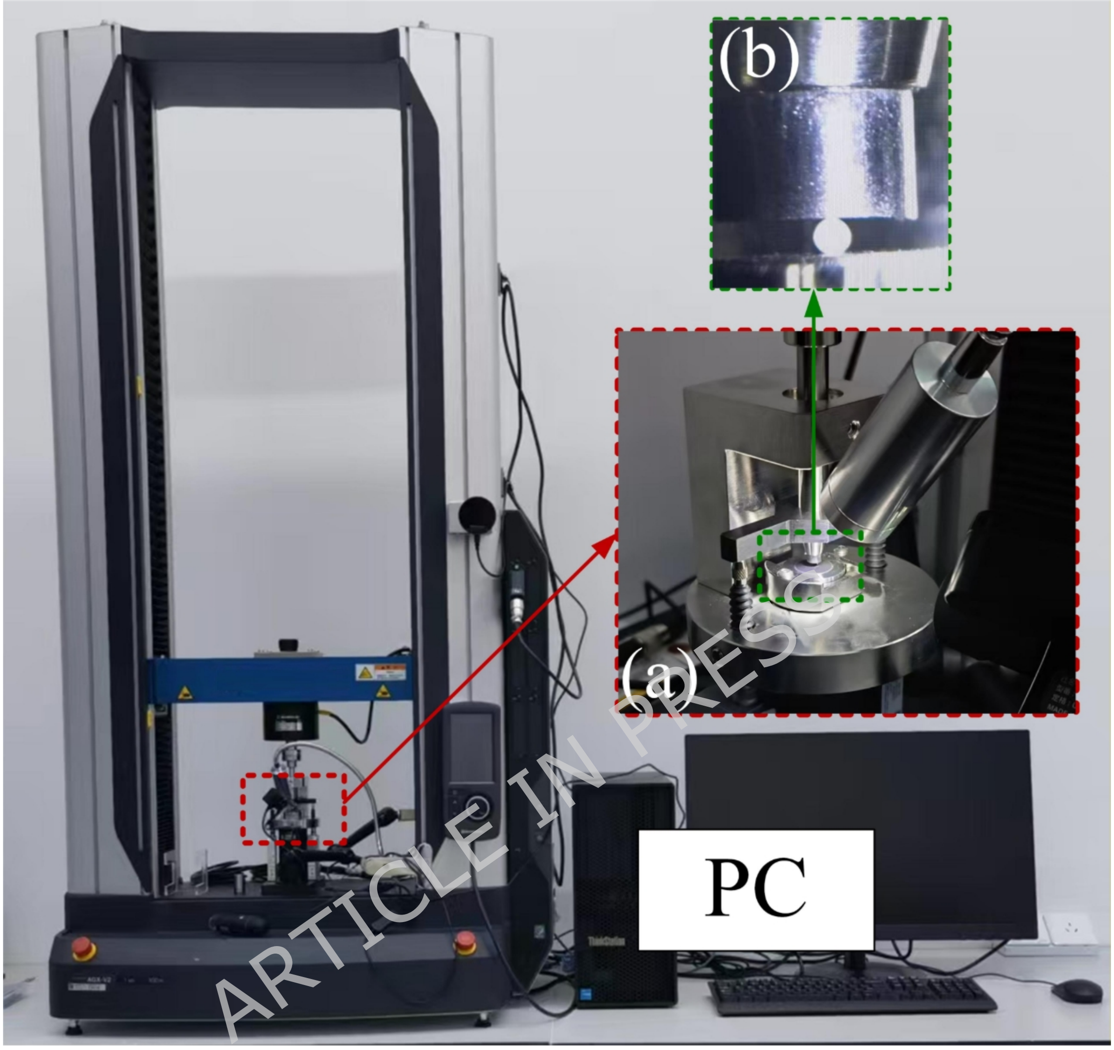

Fig. 2. Crushing Test Apparatus: (a) Detailed view of the crushing device, (b) Crushing test in progress.

In the formal experiments, six groups of zirconia ceramic microspheres with different diameter ranges were selected, with 10 particles tested in each group to obtain their force–displacement curves. The particle diameter ranges for Groups 1 to 6 were 0.1–0.2 mm, 0.2–0.3 mm, 0.3–0.4 mm, 0.4–0.6 mm, 0.6–0.8 mm, and 0.8–1.0 mm, respectively. As shown in Fig. 3a, microspheres with different diameters are presented. In addition to the mechanical tests, the remaining microspheres were characterized by scanning electron microscopy (SEM) to evaluate their sphericity (circularity), defined as $C = 4\pi A/P^2$, where A is the projected area and P is the projected perimeter. For each size group, 15 microspheres were selected for measurement. The parameter C characterizes the projected circularity and was used as a quantitative criterion for near-spherical geometry, combined with multi-particle statistical analysis. The results are summarized in Table 2, from which it can be observed that the smallest diameter group exhibits relatively poorer sphericity. Figure 3c shows representative SEM images of microspheres from the smallest size group with the lowest sphericity. The particles with noticeably rough surfaces are impurity particles rather than zirconia ceramic microspheres.

Table 2

Sphericity range of microspheres with different sizes

Group	Diameter range (mm)	Sphericity range
1	0.8-1.0	0.955-0.989
2	0.6-0.8	0.951-0.990
3	0.4-0.6	0.940-0.985
4	0.3-0.4	0.937-0.982
5	0.2-0.3	0.926-0.974
6	0.1-0.2	0.892-0.947

Since the diameter of each ceramic microsphere was not strictly uniform, individual measurements were required for each specimen. The diameter was determined by recording the displacement at the moment when the applied load exceeded 0.5 N and subtracting this displacement from the initial gap, yielding the actual particle diameter. In addition, the microsphere diameters were independently measured by scanning electron microscopy (SEM) to validate the instrument-based measurements.

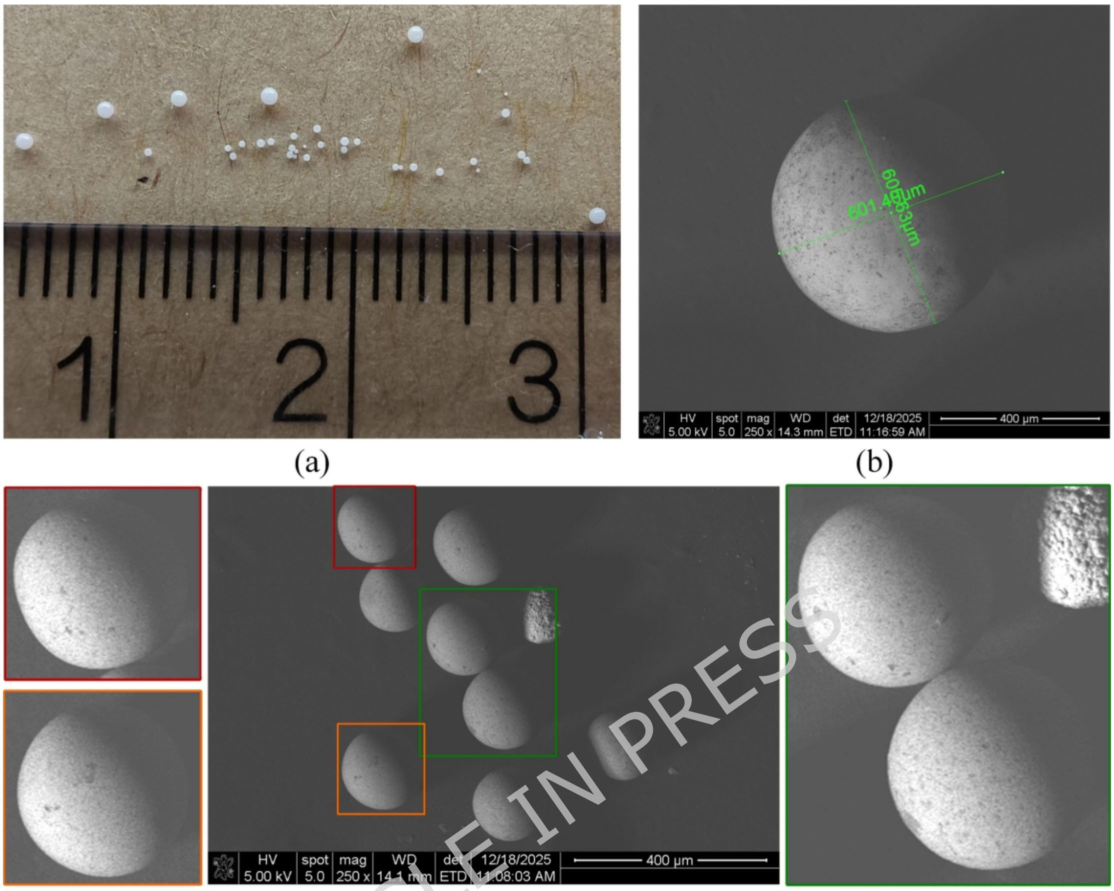

(a) (b)

(c)

Fig. 3. Ceramic microspheres: (a) different diameters; (b) diameter measurement under microscope; (c) SEM image of microspheres in the smallest size group.

2.2. Analysis of Experimental Results

2.2.1. Strength Testing of PCD Composite Plates

As shown in Fig. 4, to evaluate the actual performance of the indenter made from PCD, a comparative test was conducted using a 9 mm diameter ZrO_2 ceramic sphere on an 880/10T high- and low-temperature testing machine. The experimental procedures are illustrated in Fig. 5a and Fig. 5b, where the ceramic sphere was crushed directly using a metallic indenter and between two PCD composite plates, respectively. The corresponding results are presented in Fig. 6. During the crushing of this high-hardness ceramic sphere, the difference in the force–displacement curves obtained from the metallic and PCD indenters primarily resulted from plastic deformation occurring at the contact area between the metallic indenter and the ceramic sphere. As shown in Fig. 6a, the metallic indenter exhibited obvious plastic deformation after the test, with a permanent indentation formed at the bottom. In contrast, the surface of the PCD composite plate only underwent minor elastic deformation during the crushing process, as shown in Fig. 6b, and retained its mirror-like finish without any plastic deformation. Consequently, the force–displacement curve measured using the PCD plates demonstrated significantly higher accuracy compared to that obtained with the conventional hard metal indenter.

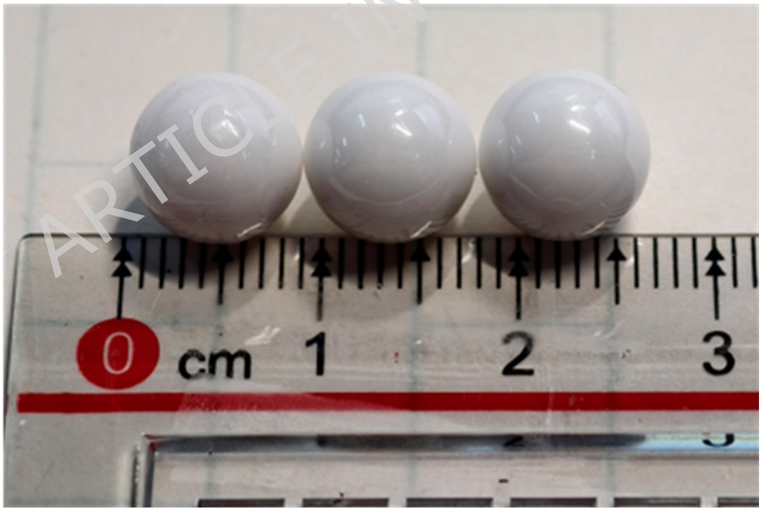

Fig. 4. Ceramic spheres used in the comparative experiment

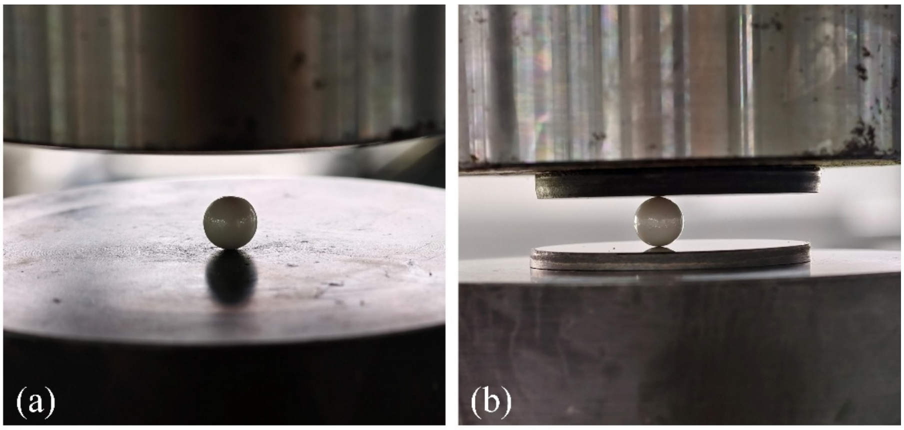

Fig. 5. Comparative test of indenters used in the crushing experiment: (a) Carbide Indenter, (b) PCD Composite Indenter.

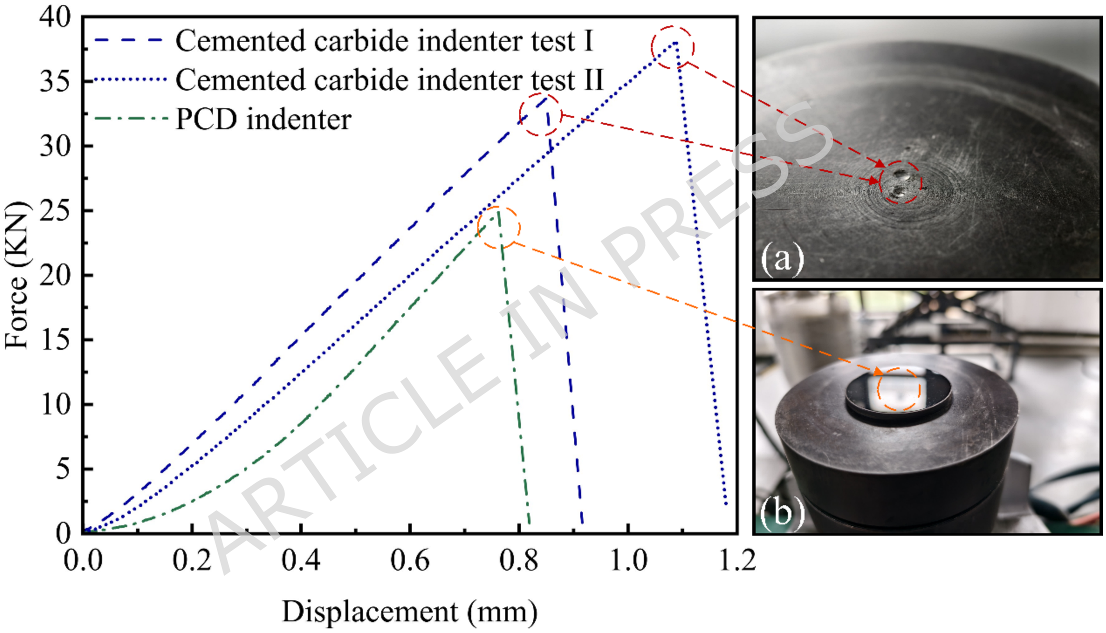

Fig. 6. Crushing Test Results and Indenter Deformation for 9 mm ZrO_2 Ceramic Ball Using Different Indenters: (a) Carbide Indenter, (b) PCD Composite Indenter

2.2.2. Analysis of Crushing Test Results

As described in Section 2.1, the 60 zirconia ceramic microspheres were divided into six groups (Groups 1–6). The force–displacement curves obtained from the crushing tests are presented in Fig. 7. In the group with diameters ranging from 0.1 to 0.2 mm, two curves exhibited noticeable deviations, and the overall trend of this group differed from that of the others. This discrepancy arises because the test requires microspheres with sufficiently high sphericity. As indicated by Table 2, the smallest microspheres are more difficult to manufacture with high geometric precision; consequently, a small fraction of particles in Group 1 exhibit noticeably reduced sphericity due to processing limitations. This insufficient sphericity degraded the quality of the corresponding force–displacement curves, and two curves showed clear anomalies. Therefore, these two curves were excluded from all subsequent analyses. For clarity in the following discussion, the following definitions are introduced: let l denote the displacement of the loading platen from the moment of contact with the ceramic microsphere to any point before fracture occurs. Let L_1 represent the displacement of the platen from the moment of contact to the instant of fracture, defined as the fracture displacement. The corresponding maximum load on the force–displacement curve is referred to as the fracture load or crushing load, denoted as F_f, and D denotes the diameter of the microsphere. An analysis of the force–displacement curves indicates a high degree of scatter within individual diameter groups. For particles with the same nominal diameter, the fracture displacement, fracture load, and the slope of the force–displacement curve varied considerably. This variation was especially pronounced in the group with the smallest diameters, where the curves exhibited the most significant scatter.

For each particle size group, the average diameter and average fracture load of the zirconia microspheres were calculated. Based on these values, a plot of the average maximum cross-sectional area versus the average fracture load was generated, as shown in Fig. 8.

It can be observed that each data point of the average fracture load versus the average maximum cross-sectional area lies very close to the fitted line, with an average percentage error of only 4.92%. Therefore, the fracture load can be considered proportional to the square of the diameter, indicating a strong size dependence of the failure load for zirconia microspheres.

The ratio of the fracture displacement to the particle diameter is defined as the compression diameter ratio (r_{cd}). This dimensionless parameter, expressed as, serves as $r_{cd} = L_1/D$, a normalized indicator of the relative compressive deformation sustained by a ceramic microsphere at the point of fracture.

The r_{cd} is indicative of the fracture behavior of the material and facilitates comparative analysis across particles of different sizes. A higher r_{cd} value suggests that the microsphere has undergone greater compressive deformation before failure, implying superior compressive resistance and a more robust fracture performance.

The relationships between fracture load and microsphere diameter, as well as between the compression diameter ratio (r_{cd}) and diameter, are illustrated in Fig. 9 and Fig. 10. To facilitate interpretation, statistical analyses were performed for the fracture load and r_{cd} within each microsphere size group, including the standard deviation (SD), coefficient of variation (CV), and interquartile range (interquartile range, IQR). The corresponding results are summarized in Tables 3 and 4. It can be observed that, for microspheres within the same size group, the coefficient of variation of the fracture load is generally greater than 10%, and the interquartile range is relatively large, indicating pronounced scatter. In contrast, the coefficient of variation of r_{cd} within the same group is mostly below 10%, suggesting that the dispersion of r_{cd} is slightly lower than that of the fracture load. Nevertheless, noticeable scatter remains present.

Table 3

Statistical analysis of fracture load (N) for six groups of ceramic microspheres

Group	Number of samples	Mean	SD	SV(%)	IQR
1	8	21.075	2.921	13.86	2.802
2	10	68.913	8.903	12.92	10.481
3	10	91.744	16.287	17.75	26.946
4	10	232.086	47.181	20.33	66.780
5	10	304.363	28.283	9.29	47.789
6	10	550.913	65.963	11.97	75.764

Table 4

Statistical analysis of r_{cd} for six groups of ceramic microspheres

Group	Number of samples	Mean	SD	SV(%)	IQR
1	8	0.0973375	0.0125035	12.85	0.0076525
2	10	0.128997	0.008676	6.73	0.011588
3	10	0.131589	0.010109	7.68	0.010165
4	10	0.151546	0.014351	9.47	0.021098
5	10	0.154950	0.010993	7.09	0.015302
6	10	0.183813	0.015243	8.29	0.015370

In contrast, a clear trend is observed across different microsphere size groups: both r_{cd} and fracture load increase markedly with increasing diameter. This indicates that the fracture-related mechanical performance of ceramic microspheres improves as the diameter increases.

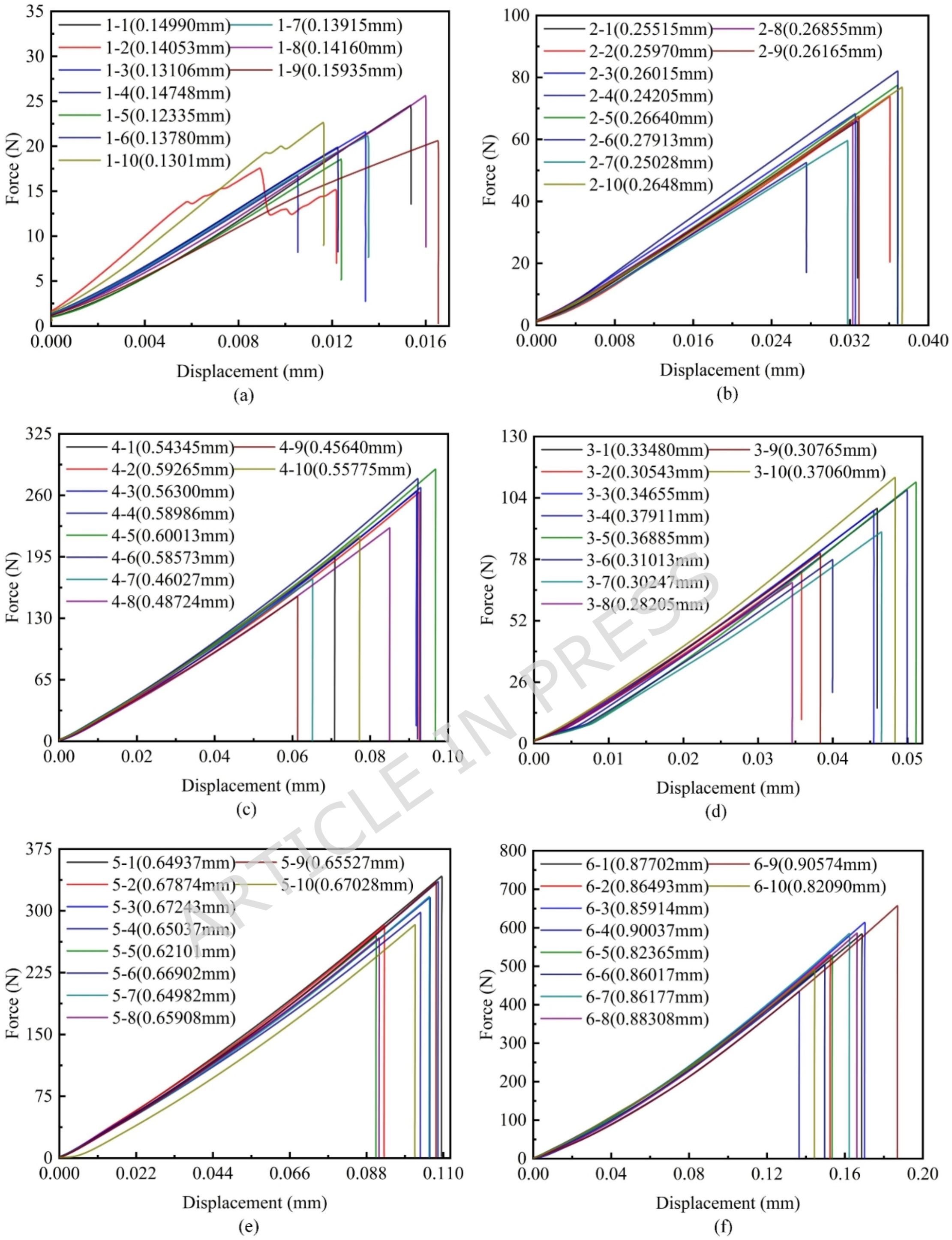

Fig. 7. Force–displacement curves from crushing tests of six groups of ceramic microspheres:

(a) Group 1, particle diameter: 0.1–0.2 mm;

(b) Group 2, particle diameter: 0.2–0.3 mm;

(c) Group 3, particle diameter: 0.3–0.4 mm;

(d) Group 4, particle diameter: 0.4–0.6 mm;

(e) Group 5, particle diameter: 0.6–0.8 mm;

(f) Group 6, particle diameter: 0.8–1.0 mm.

For ceramic materials, fracture toughness is strongly influenced by defects. We therefore infer that, for spherical particles, the specific surface area (surface area-to-volume ratio) increases as the microsphere diameter decreases. As a result, smaller microspheres exhibit a higher specific surface area, and from a statistical perspective, a higher apparent defect number density per unit volume. This interpretation is based on geometric and statistical considerations rather than on direct quantification of defect populations. Under these conditions, the contribution of defects—particularly surface defects—is effectively amplified. Consequently, during compressive loading, microspheres with smaller diameters are more prone to instability and are therefore more likely to undergo complete fracture.

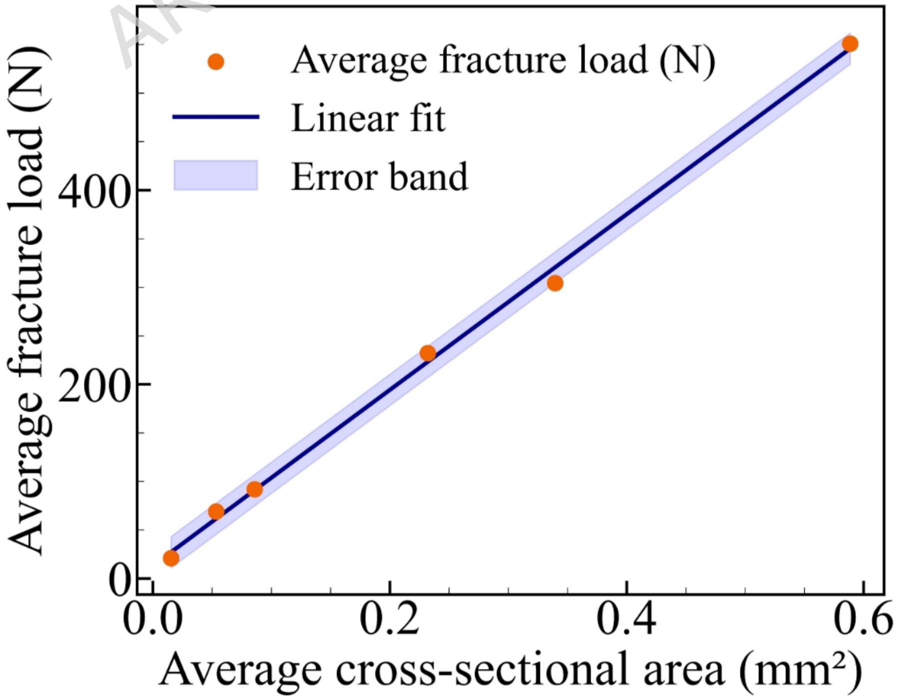

Fig. 8. Relationship between average fracture load and average maximum cross-sectional area of ZrO_2 ceramic microspheres.

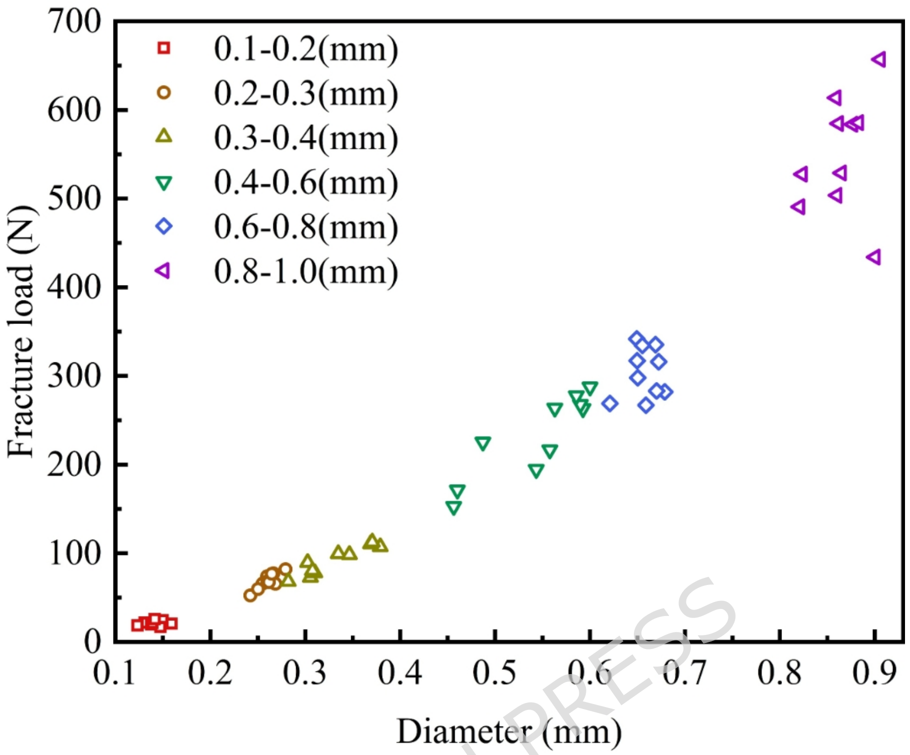

Fig. 9. Relationship between fracture load and diameter of ZrO_2 ceramic microspheres.

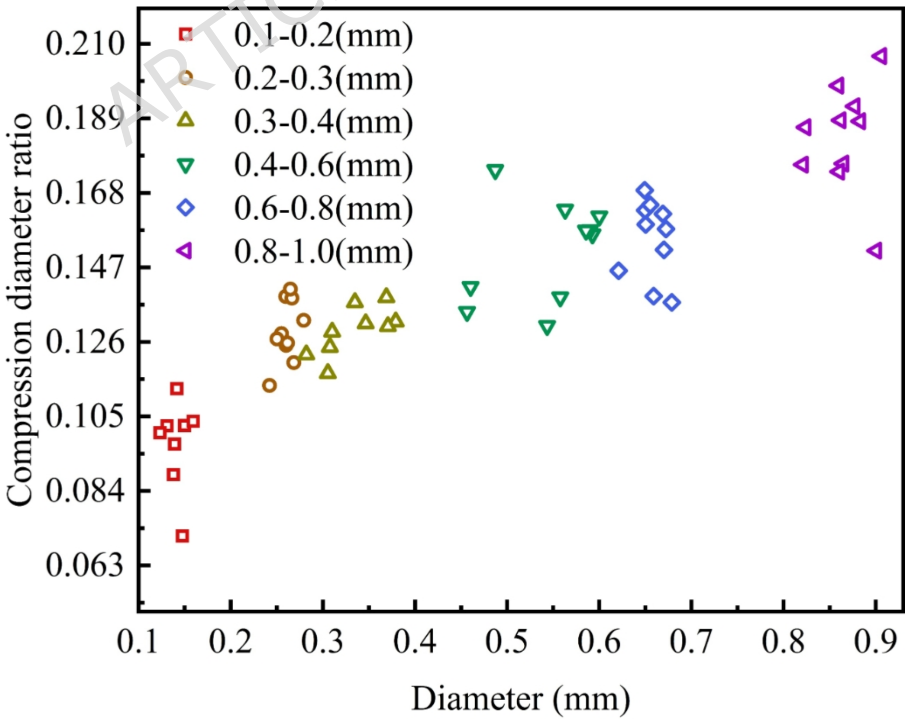

Fig. 10. Relationship between r_{cd} and diameter of ZrO_2 ceramic

microspheres.

3 Numerical Simulation

3.1. Cohesive Elements

The energy dissipation behavior of cohesive elements in this study was modeled using both the cohesive crack model and the fictitious crack model. According to the underlying assumptions, the fracture surface is subjected to opening σ_{I}, sliding σ_{II}, and tearing tractions σ_{III} .A bilinear cohesive law is adopted, which assumes a linear traction–separation relationship prior to damage initiation. Initial stiffness values K_{I}, K_{II}, and K_{III} are defined for the opening, sliding, and tearing modes, respectively. Under certain loading conditions, the cohesive elements may fail due to excessive normal or shear traction. A representative mixed-mode traction–separation law is illustrated in Fig. 11. The damage initiation criterion is typically defined by the quadratic nominal stress criterion proposed by Ye et al. [29], and its mathematical expression is given as follows:

$$\left\{\frac{\langle \sigma_{\mathrm{I}} \rangle}{S_{\mathrm{I}}}\right\}^2 + \left\{\frac{\sigma_{\mathrm{II}}}{S_{\mathrm{II}}}\right\}^2 + \left\{\frac{\sigma_{\mathrm{III}}}{S_{\mathrm{III}}}\right\}^2 = 1 \tag{1}$$

Here, $\langle \ \rangle$ denotes the Macaulay bracket, which ensures that compressive (negative) normal tractions do not contribute to damage at the cohesive interface. S_{I}、S_{II} and S_{III} represent the nominal tractions at damage initiation in opening, sliding, and tearing modes, respectively. This criterion effectively captures damage initiation under Mode I, Mode II, Mode III, and mixed-mode fracture conditions. Once damage begins, the model transitions into the damage evolution phase, which is governed by a scalar damage variable, *D*. This variable is defined as a function of the effective relative traction σ_{eff} and the effective relative displacement δ_m, and its evolution is described by the following expression:

$$D=\frac{\delta_m^f(\delta_m^{max}-\delta_m^0)}{\delta_m^{max}(\delta_m^f-\delta_m^0)},\quad \delta_m^{max}\geq\delta_m^0 \tag{2}$$

$$\delta_m^0=\sqrt{\left(\delta_{I}^0\right)^2+\left(\delta_{II}^0\right)^2+\left(\delta_{III}^0\right)^2} \tag{3}$$

$$\delta_m^f=\sqrt{\left(\delta_{I}^f\right)^2+\left(\delta_{II}^f\right)^2+\left(\delta_{III}^f\right)^2} \tag{4}$$

$$\delta_m^{max}=\sqrt{\left(\delta_{I}^{max}\right)^2+\left(\delta_{II}^{max}\right)^2+\left(\delta_{III}^{max}\right)^2} \tag{5}$$

Here, δ_{max} denotes the maximum effective displacement attained during loading, δ^0 represents the displacement at damage initiation, and δ^f corresponds to the displacement at complete failure.

The evolution of the damage variable *D* results in the progressive degradation of stiffness and traction across all three fracture modes, ultimately leading to complete failure.

$$\sigma_{I}=\begin{cases}(1-D)K_{I}\delta_{I}, & \delta_{I}\geq 0\\ K_{I}\delta_{I}, & \delta_{I}<0\end{cases} \tag{6}$$

$$\sigma_{II}=(1-D)K_{II}\delta_{II} \tag{7}$$

$$\sigma_{III}=(1-D)K_{III}\delta_{III} \tag{8}$$

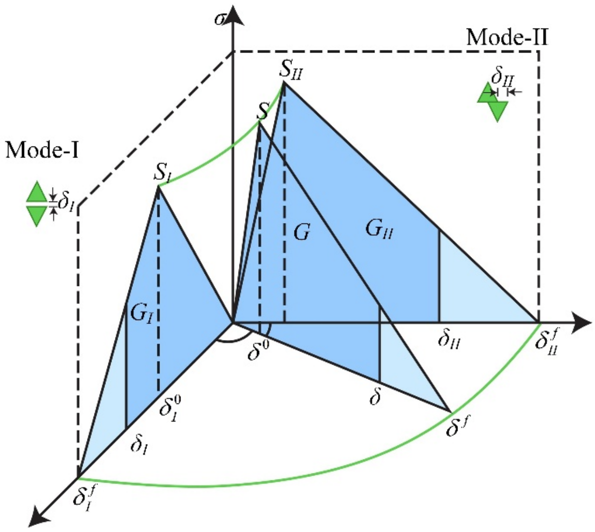

Fig. 11. Schematic diagram of the traction–separation law.

According to the findings of de Oliveira [30], the combination of the Benzeggagh–Kenane (BK) failure criterion [23] with the quadratic stress initiation criterion yields smaller stiffness errors. Therefore, the BK failure criterion was adopted in this study.

BK criterion is：

$$G_c^{max} = G_I + \left(G_{IIc} - G_{Ic}\right)\left(\frac{G_{II}}{G_c}\right)^{\eta} + \left(G_{IIIc} - G_{Ic}\right)\left(\frac{G_{III}}{G_c}\right)^{\eta} \tag{9}$$

$$G_c = G_I + G_{II} + G_{III} \tag{10}$$

Here, G_c denotes the total energy release rate, G_I represents the energy release rate in the opening mode, while G_{II} and G_{III} correspond to the energy release rates in the sliding and tearing modes, respectively. G_{Ic}, G_{IIc}, and G_{IIIc} refer to the critical fracture energies for the opening, sliding, and tearing modes, respectively.

3.2. Construction of the Finite Element Model

A finite element model was developed to simulate the crushing behavior based on the experimental setup, ensuring consistency with the actual test conditions. The simulation focused on ceramic microspheres with diameters ranging from 0.8 mm to 1.0 mm, using the average diameter of 0.86 mm as the representative modeling value. The upper indenter and lower support plate were simplified as two identical rectangular blocks, each measuring 0.9 mm × 0.9 mm × 0.15 mm.

To replicate the loading conditions observed in the experiment, the lower support plate was fully constrained, while the upper indenter was driven downward at a constant displacement of 0.3 mm, simulating the crushing process under quasi-static conditions.

In terms of meshing, the upper and lower platens were discretized using C3D8R elements. To closely replicate the actual crushing process, the surface of the ceramic sphere was first partitioned using a Voronoi tessellation (also known as the Voronoi diagram).

The Voronoi tessellation exhibits three fundamental properties: each Voronoi cell contains exactly one discrete site; all points within a Voronoi cell are closest to its associated site and every point on the boundary between two cells is equidistant to the two adjacent sites.

Based on the principles of Voronoi tessellation and practical experience in mesh generation, discrete seed points with an average spacing of 0.235 mm were distributed on the microsphere surface. A custom algorithm was employed to construct the corresponding Voronoi cells according to the spatial arrangement of these points, as illustrated in Fig. 12a. This tessellation approach enabled the mesh to be randomly distributed across the sphere's surface, as shown in Fig. 13a, rather than forming a regular pattern as in Fig. 13b. Such randomization ensures that cohesive elements are uniformly and stochastically distributed, thereby enabling a high-fidelity simulation of the fracture behavior of ceramic microspheres.

As shown in Figs. 14a and 14b, the mesh generated using Voronoi tessellation exhibits a more random and physically realistic fracture pattern, whereas the cracks produced by the default meshing approach appear highly artificial, with some even propagating vertically downward along the Z-axis.

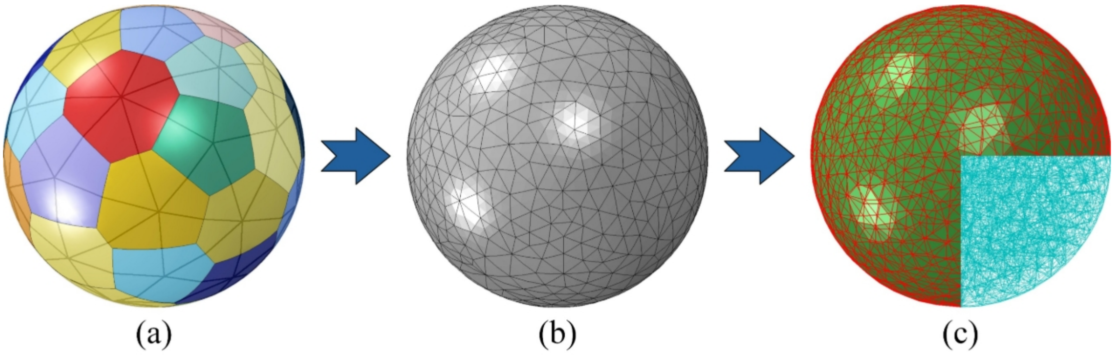

Fig. 12. Numerical modeling of the ceramic microsphere: (a) Surface discretized by Voronoi tessellation; (b) Mesh generation; (c) Insertion of zero-thickness cohesive elements into the mesh.

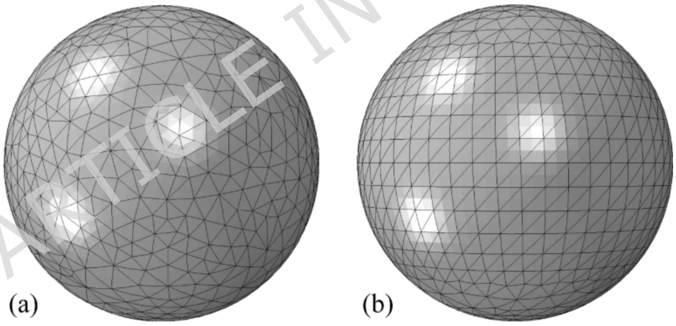

Fig. 13. Mesh Generation Diagram for Numerical Simulation (a) Mesh of the microsphere after Voronoi partitioning; (b) Mesh of the microsphere generated using the default method.

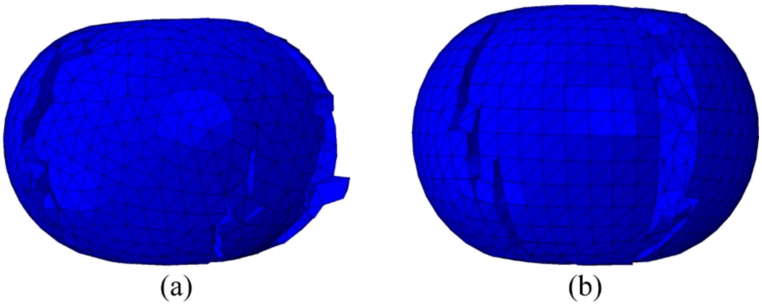

Fig. 14. Comparison of numerical crushing simulations: (a) mesh of the microsphere generated by Voronoi tessellation; (b) mesh of the microsphere generated by the default method.

After the surface of the microsphere was partitioned using Voronoi tessellation, the interior volume was discretized with C3D4 elements (Fig. 12b), into which COH3D6 cohesive elements were embedded (Fig. 12c). Since the in-plane thickness of the COH3D6 elements is zero, the geometry of the mesh remains unaffected. Each finite element is capable of undergoing localized deformation in response to nodal forces, and in regions where cracks initiate, the traction–separation law allows for both crack initiation and propagation.

According to the findings of De Maio et al. [31], the density of cohesive elements has negligible influence on the global force–displacement response, affecting only the detailed crack propagation path. To verify this conclusion, the force–displacement curves of two microsphere models were compared: one consisting of 35,498 C3D4 elements and 69,025 COH3D6 elements, and another composed of 10,882 C3D4 elements with 31,886 embedded COH3D6 elements. In addition, to evaluate whether the mesh density influences the force–displacement behavior under elastic contact, three purely elastic models with 1,849, 10,882, and 134,098 C3D4 elements were analyzed and their force–displacement curves were compared. The detailed mesh configurations and element types are shown in Fig. 15a, and the corresponding results are presented in Fig. 15b. The results clearly indicate that the mesh density has a negligible effect on the force–displacement response of elastic bodies. Considering that an excessively coarse mesh may compromise crack-path accuracy, while an overly fine mesh substantially increases computational cost, a model comprising 10,882 C3D4 elements and 31,886 COH3D6 elements was ultimately selected for subsequent simulations.

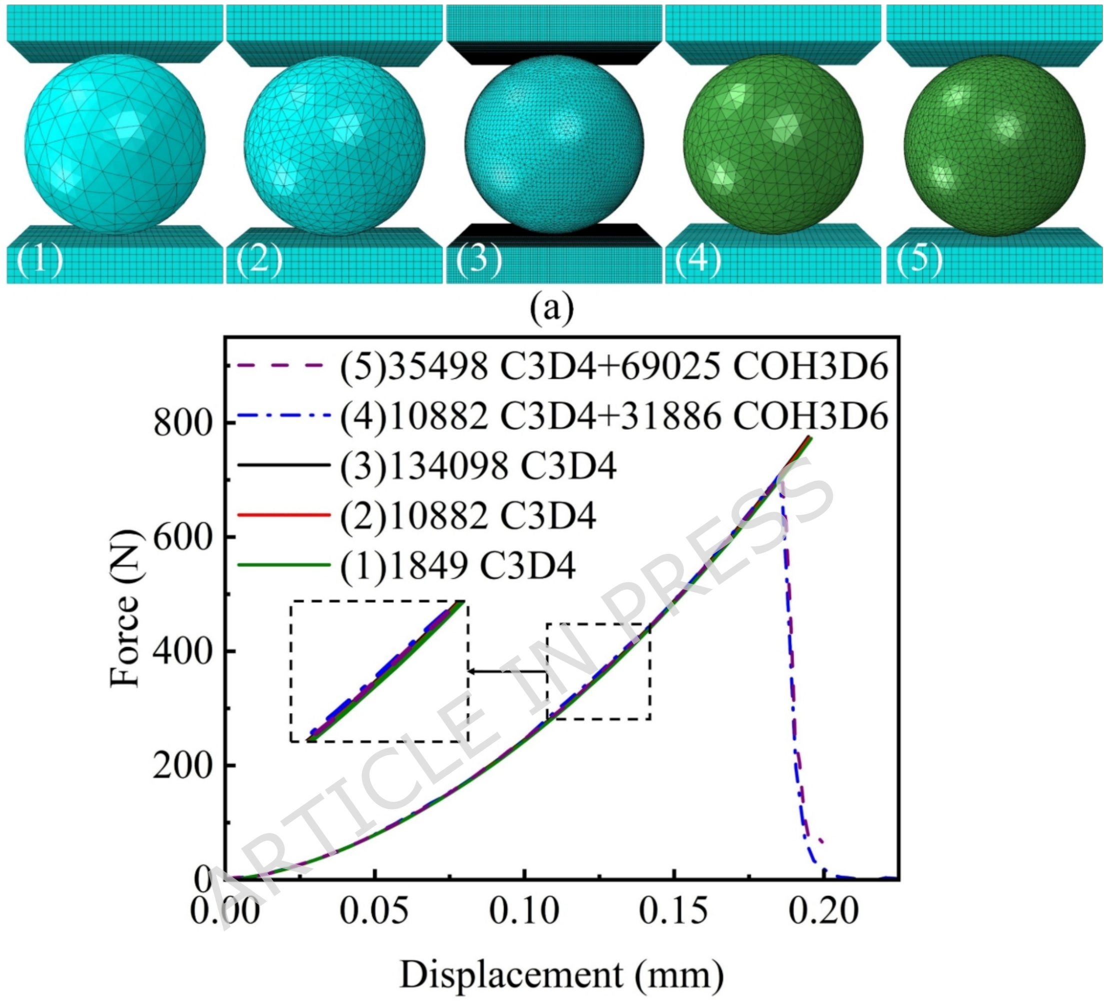

(a)

(b)

Fig. 15. Numerical simulations with different mesh densities: (a) finite element models; (b) corresponding force–displacement curves.

The parameters assigned to the mesh are listed in Tables 5–9. Among them, the data in Table 5 were derived from Table 1. The elastic modulus E of the zirconia solid elements was selected within the range reported in Table 1, while the Mode I fracture energy of the cohesive elements was determined based on linear elastic fracture mechanics using the relationship between fracture toughness and fracture energy, $G_{Ic}=(K_{Ic})^2/E$. The relationships among the traction–separation laws under mixed-mode loading were adopted with reference to relevant literature [23,31]. The friction coefficient between the PCD plates and ZrO_2 ceramic was set to 0.12, based on the experimental findings reported by Liao [12].

Table 5

Material Properties of PCD Solid Elements

Parameter	Symbol	Value
Density	$\rho(Kg/m^3)$	7890
Elastic Modulus	$E(GPa)$	919
Poisson’s Ratio	υ	0.09

Table 6

Material Properties of ZrO_2 Solid Elements-1

Parameter	Symbol	Value
Density	$\rho(kg/m^3)$	5860
Elastic Modulus	$E(GPa)$	224
Poisson’s Ratio	υ	0.3

Table 7

Cohesive Element Parameters-1

Parameter	Symbol	Value
Normal stiffness	$K_I\,(N/mm^2)$	5×10^7
First shear stiffness	$K_{II}\,(N/mm^2)$	5×10^7
Second shear stiffness	$K_{III}\,(N/mm^2)$	5×10^7
Tensile strength	$S_I\,(GPa)$	2.307
First shear strength	$S_{II}\,(GPa)$	3.23
Second shear strength	$S_{III}\,(GPa)$	3.23

Mode I fracture energy	$G_I\,(N/mm)$	0.2645
Mode II fracture energy	$G_{II}\,(N/mm)$	0.3703
Mode III fracture energy	$G_{III}\,(N/mm)$	0.3703

Table 8

Material Properties of ZrO_2 Solid Elements-2

Parameter	Symbol	Value
Density	$\rho(kg/m^3)$	5860
Elastic Modulus	$E(GPa)$	210
Poisson’s Ratio	υ	0.3

Table 9

Cohesive Element Parameters-2

Parameter	Symbol	Value
Normal stiffness	$K_I\,(N/mm^2)$	5×10^7
First shear stiffness	$K_{II}\,(N/mm^2)$	5×10^7
Second shear stiffness	$K_{III}\,(N/mm^2)$	5×10^7
Tensile strength	$S_I\,(GPa)$	1.702
First shear strength	$S_{II}\,(GPa)$	2.383
Second shear strength	$S_{III}\,(GPa)$	2.383
Mode I fracture energy	$G_I\,(N/mm)$	0.1449
Mode II fracture energy	$G_{II}\,(N/mm)$	0.2029
Mode III fracture energy	$G_{III}\,(N/mm)$	0.2029

3.3. Results and Analysis

3.3.1. Analysis of Stress and Strain Distributions

Before the failure of the ceramic microsphere, a monotonically increasing uniaxial compressive load is applied as the PCD platen descends. Throughout this process, all deformation remains within the linear elastic regime. Therefore, a finite element simulation without cohesive elements, based on linear elasticity, can accurately capture the stress and strain distributions within the microsphere.

Since strain concentration can lead to crack initiation, Fig. 16. and Fig. 17. present the maximum strain distribution captured from finite element simulations, as well as the strain distributions along both the horizontal direction (parallel to the compression plates) and the vertical direction (perpendicular to the plates) at various displacement stages. In these figures, red regions indicate strain concentrations caused by tensile stress, while blue regions indicate those induced by compressive stress. The maximum strain is clearly distributed along the vertical axis, with the highest compressive strain concentrated in the contact area between the compression plates and the microsphere, spreading inward toward the center. The maximum tensile strain appears along the horizontal axis near the edge of the sphere, which results from the elastic outward deformation of the sphere’s boundary due to the applied compressive force. In the horizontal direction, compressive strain concentrations mainly occur at the edge of the contact area with the plates. Tensile strain, on the other hand, is concentrated at the central region of the two hemispheres along the horizontal section. This is attributed to the vertical compression causing lateral expansion, generating significant horizontal tensile strain, primarily distributed along the vertical axis. In contrast, the vertical strain distribution is notably different. Compressive strain near the contact area exhibits a fan-shaped spread toward the sphere’s center. As the compression head continues to descend, tensile strain gradually shifts outward toward the microsphere's edge, decreasing as it approaches the vertical axis.

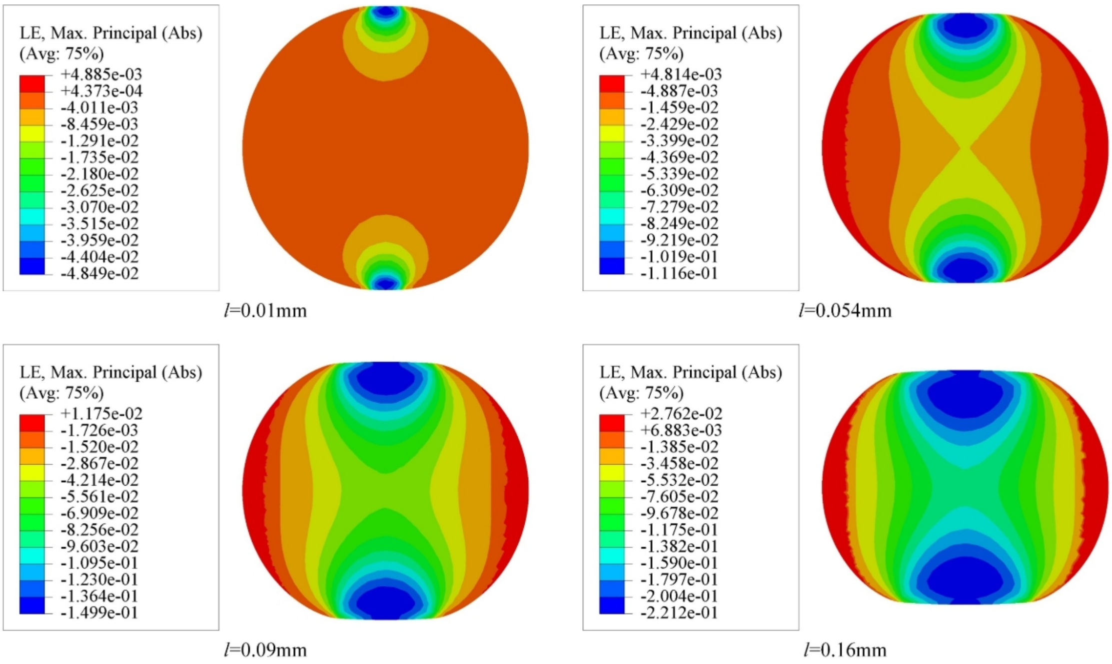

Fig. 16. Distribution of maximum strain at different indenter displacements (l).

The distributions of principal stress across the maximum cross section and surface pressure of the ceramic microsphere are shown in Fig. 18. The cross-section perpendicular to the loading platen corresponds to the vertical plane, while the one parallel to the platen corresponds to the horizontal plane. In the vertical section, the internal stress resultant manifests as tensile stress acting outward and perpendicular to the cross-sectional surface, while the externally applied load induces axial compressive stress. At relatively low loads, the internal stress within the ceramic sphere remains minimal, with slightly elevated stress appearing beneath the contact region. As the load increases monotonically, the stresses near the contact region become significantly higher than those inside the sphere, while the internal stress field remains relatively uniform. Moreover, due to the elevated internal stress, once an initial crack appears, it rapidly propagates throughout the microsphere, leading to catastrophic failure.

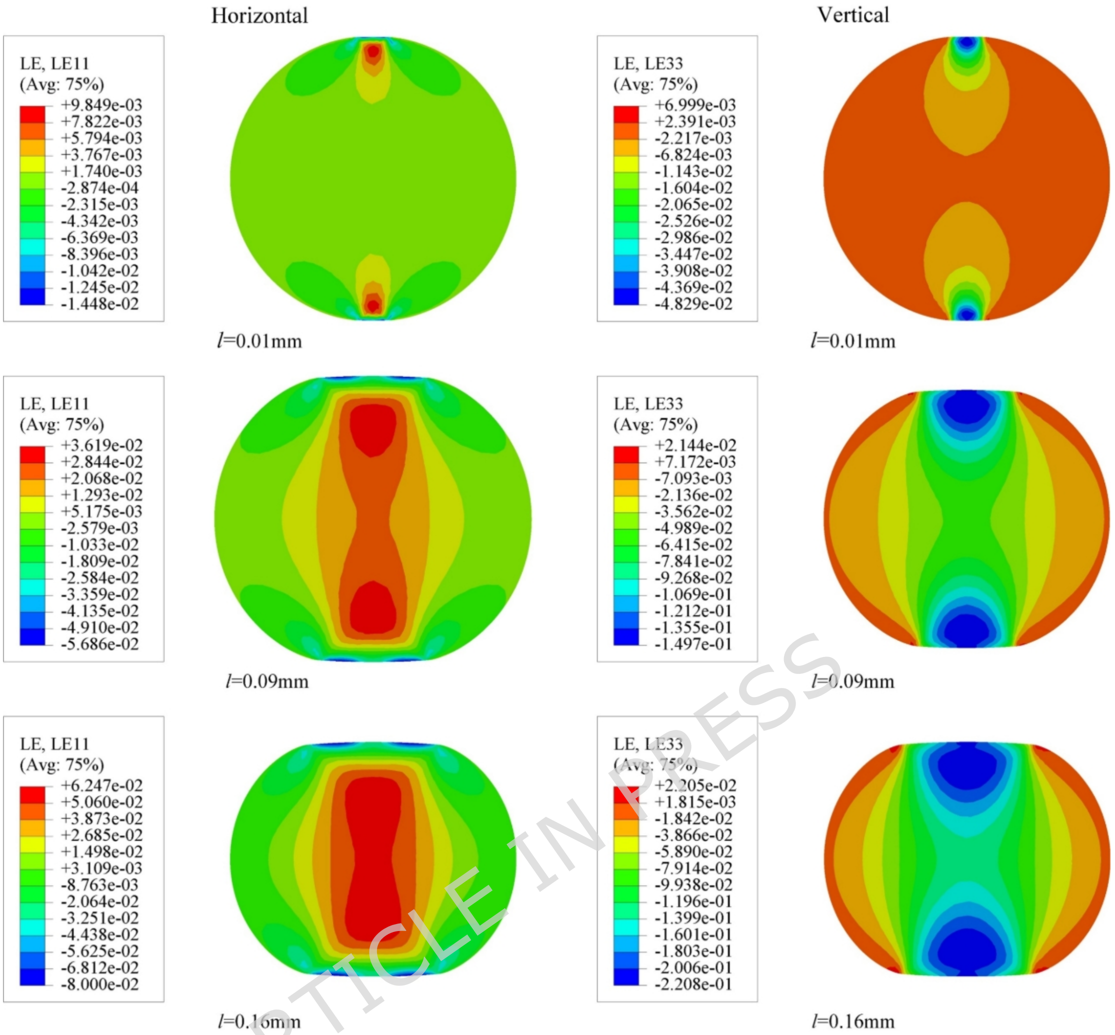

Fig. 17. Strain distribution in horizontal and vertical directions at different indenter displacements (*l*).

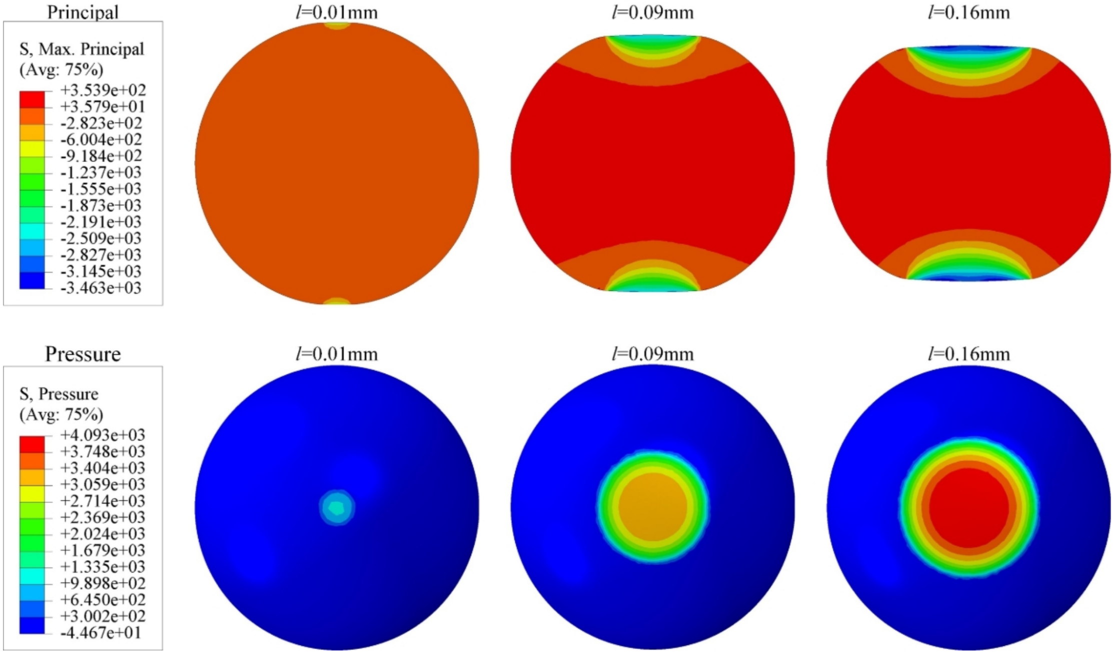

Fig. 18. Stress distribution at different indenter displacements (*l*).

3.3.2. Analysis and Discussion of the Crushing Process

For brittle materials, the presence of local defects such as pores, pre-existing cracks, or nonuniform grain boundaries leads to stress concentration and the formation of crack tips, which induce localized tensile stresses. Under high compressive loads, the material tends to develop microcracks along planes of maximum shear stress, resulting in crushing failure. Unlike metals, brittle materials cannot relieve stress through dislocation motion and are extremely sensitive to microdefects. Once local instability occurs, cracks propagate rapidly, leading to catastrophic fragmentation. Specifically, for the zirconia microspheres investigated in this study, the internal stress analysis presented in the previous section indicates that the initial cracks originate near regions subjected to high contact stresses. Once crack initiation occurs, the compressive stresses within the microsphere drive rapid crack propagation, ultimately causing complete failure of the particle.

Cohesive elements are well-suited for simulating the fracture processes of brittle and quasi-brittle materials. The corresponding simulation results are shown in Fig. 19, where the brown regions in Fig. 19a represent cohesive elements that have fully failed. Within the initial 95% of the total fracture displacement, no damage is observed within the ceramic microsphere. At approximately 95.7% of the fracture displacement (Point 2), the first micro-crack initiates. During the final 0.5% increment in displacement (Point 3), the cohesive elements surrounding the microcrack experienced complete damage, leading to internal structural instability. This instability caused the crack to rapidly propagate through the entire microsphere, resulting in complete fracture and a sharp drop in the force–displacement curve. The location of the first crack initiation within the cohesive zone precisely corresponds to the region of maximum stress and strain overlap, which is consistent with widely accepted failure criteria. As the loading platen continues to displace, more cohesive elements reach their critical damage thresholds, triggering a rapid and unstable crack propagation through the entire sphere. This results in the complete collapse of the microsphere, as indicated by the abrupt decline in the force–displacement response, consistent with the experimental observations.

The fracture energies G_I, G_{II}, and G_{III} defined in the cohesive elements represent the mode I, mode II, and mode III fracture energies of the material, respectively, i.e., G_{Ic}, G_{IIc}, and G_{IIIc}. When combined with the material properties of the bulk solid elements, a reasonable fracture toughness K_{Ic} can be obtained. As shown in Fig. 19, the simulated force–displacement curves based on the material properties are compared with an experimental result. The parameters listed in Tables 6-9 yield simulated curves that accurately capture both the fracture load and fracture displacement of experimental curves 6–4 and 6-9. This demonstrates that incorporating cohesive elements into the finite element model can effectively reproduce the entire flat-plate crushing process. With appropriate tuning of material parameters, the simulation can achieve fracture displacement and fracture load values that closely match those observed in the experiment. Because the two force–displacement curves nearly overlap prior to fracture and the corresponding microspheres have almost identical diameters, the elastic moduli of microspheres 6-4 and 6-9 are expected to be similar. However, numerical simulations cannot fully capture the elastic deformation of the microspheres, and the experimental specimens are not perfect spheres. These factors lead to slightly higher measured loads in the experiments than those predicted by the simulations at the same displacement. Based on the data summarized in Tables 1, 6, and 8, the present method yields an error of approximately 5% in the prediction of the elastic modulus.

By substituting the simulated elastic modulus and fracture energy into the fracture toughness equation：

$$K_{Ic} = \sqrt{G_{Ic} \cdot E} \tag{11}$$

the values of the two microspheres were calculated to be 5.516 MPa·m$^{0.5}$ and 7.633 MPa·m$^{0.5}$, respectively. Considering that curves 6-4 and 6-9 correspond to the minimum and maximum fracture loads among the experimental force–displacement results, the calculated values show good agreement with the data reported in Section 2.1 (5.2–8.1 MPa·m$^{0.5}$). Therefore, by calibrating the parameters in the numerical simulation, the simulated force–displacement curves can be effectively matched with the experimental ones, enabling a reasonable estimation of the mechanical properties of the ceramic microspheres.

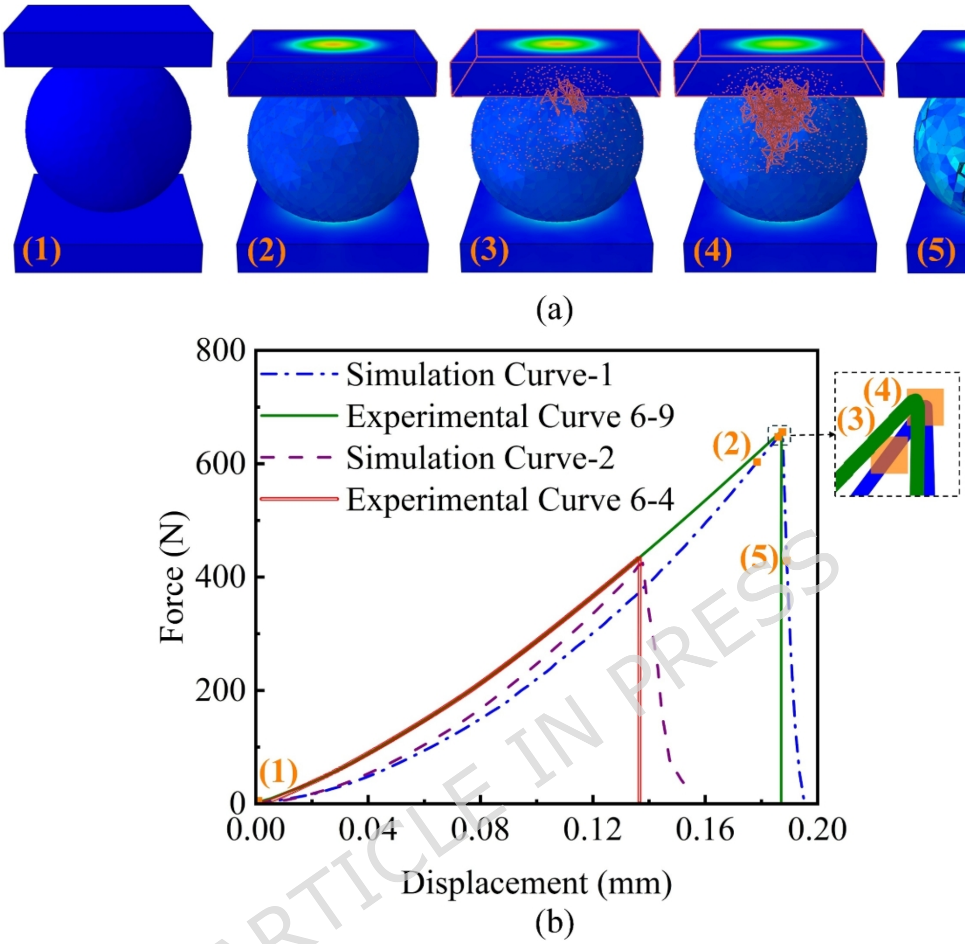

(a)

(b)

Fig. 19. Damage evolution of the microsphere during indenter displacement: (a) internal damage state; (b) corresponding force–displacement curve.

Compared with conventional methods such as the C-sphere method, the notched ball method, and the ball-on-three-balls (B3B) test, the proposed approach imposes a certain requirement on the sphericity of ceramic particles; therefore, when the sample sphericity is insufficient, the applicability of the method is limited. In addition, because polycrystalline diamond is not suitable for high-temperature environments, the present approach cannot be used to characterize the mechanical properties of ceramic microspheres at elevated temperatures. However, under non-high-temperature conditions, preparing standard test specimens for conventional methods is considerably more cumbersome, especially when the small size range of ceramic microspheres is taken into account. Obtaining qualified specimens and conducting reliable experiments therefore become much more challenging. Moreover, the large scatter commonly observed in the fracture toughness of ceramics further increases the difficulty of determining the mechanical properties of ceramic microspheres using traditional approaches. In contrast, for ceramic microspheres with sufficiently high sphericity, the proposed method is simple and efficient. During the experimental stage, in situ measurements can be performed directly on individual microspheres, allowing rapid and accurate acquisition of force–displacement curves. With respect to mechanical property evaluation, relatively accurate parameters such as elastic modulus and fracture toughness can be obtained by calibrating the force–displacement response. Furthermore, the present method can be extended by incorporating deep learning techniques to analyze crushing force–displacement curves of ceramic microspheres with different materials and sizes, thereby enabling a rapid and convenient determination of their mechanical properties.

In summary, the use of PCD platens in the flat-plate crushing test effectively overcomes the limitations of conventional setups in evaluating high-hardness ceramic spheres, enabling reliable experimental results. Meanwhile, the numerical model incorporating global cohesive zone elements accurately simulates the fracture process of ceramic microspheres under PCD platen loading. The simulated force–displacement curves exhibit strong agreement with experimental data, demonstrating that, by calibrating the model parameters, the mechanical properties of ceramic microspheres can be reasonably estimated through simulation.

4. Conclusions

This study proposes a new methodology for investigating the crushing mechanics of ceramic microspheres by combining an improved flat-plate crushing test with numerical simulations based on global cohesive zone elements. This approach provides a new perspective for evaluating the mechanical properties of ceramic microspheres, which are widely used but currently lack established experimental methods or predictive models. A dedicated experimental system was designed and constructed specifically for ceramic microspheres. By utilizing the extremely high hardness, isotropy, and ultra-low surface roughness of cost-effective PCD, the limitations of conventional flat-plate crushing tests—particularly the inaccuracy caused by insufficient indenter performance—were successfully addressed. The PCD platens transformed complex elastic–plastic contact problems into elastic–elastic contact. The advantages of PCD platens over traditional tungsten carbide platens were verified using zirconia ceramic spheres with a diameter of approximately 9 mm. Subsequently, this high-precision system enabled the accurate acquisition of force–displacement curves for sub-millimeter zirconia microspheres. Experimental results indicated that the fracture resistance of the zirconia microspheres increases with particle diameter. Based on the experimental setup, the brittle crushing process of ceramic microspheres was simulated using a Voronoi-based meshing strategy and global cohesive zone elements governed by a bilinear traction–separation law. The stress and strain distributions during the crushing process were analyzed, and the critical failure zones were identified. Finally, the crushing force–displacement curves obtained from the numerical model were consistent with experimental data, allowing for the reliable determination of elastic modulus and fracture toughness of the ceramic microspheres.

Data availability

All data generated or analyzed during this study are included in this published article.

Authors' contributions

Haojun Ma: Writing – original draft, Visualization, Validation, Software, Methodology, Investigation, Formal analysis.

Junnan Lv: Writing – review & editing, Supervision, Resources, Project administration, Methodology, Investigation, Funding acquisition, Data curation, Conceptualization.

Yubo Zhou: Visualization, Software, Resources.

Yingxuan Dong: Writing – review & editing, Supervision.

Yingzheng Song: Investigation.

Qun Li: Writing – review & editing, Supervision, Methodology, Funding acquisition, Conceptualization.

Funding

This work was supported by the National Natural Science Foundation of China (Nos. 12202426, U21B2058)

Acknowledgements

This work was supported by the National Natural Science Foundation of China (Nos. 12202426, U21B2058). This work was supported by the Postdoctoral Fellowship Program of

CPSF under Grant (GZC20241366), the funding from the Aeronautical Science Foundation of China (2024Z061070001), the Fundamental research funds for the central universities (xzy012025038), and the funding from Shaanxi Natural Science Foundation (2025JC-YBQN-071). This paper has received funding from the China Scholarship Council.

References

1. Börger A, Supancic P, Danzer R (2002) The ball on three balls test for strength testing of brittle discs: stress distribution in the disc. J. Eur. Ceram. Soc. 22.9-10, 1425-1436.
2. Wereszczak AA, Kirkland TP, Jadaan OM (2007) Strength Measurement of Ceramic Spheres Using a Diametrally Compressed "C-Sphere" Specimen. J. Eur. Ceram. Soc. 90.6, 1843-1849.
3. Supancic P, Danzer R, Witschnig S, et al (2009) A new test to determine the tensile strength of brittle balls—the notched ball test. J. Eur. Ceram. Soc. 29.12, 2447-2459.
4. Liu H, Jia L (2023) Effect of boundary conditions on tensile bending strength of glass under four-point bending. Constr. Build. Mater. 384, 131479.
5. Han X, Xiao Q, Cui K, et al (2023) Determining the fracture toughness of quasi-brittle materials with notched four-point bending tests. Eng. Frac.t Mech. 284: 109259.
6. Bassali WA (1957) The transverse flexure of thin elastic plates supported at several points. Math. Proc. Camb. Philos. Soc. Vol. 53. No. 3. Cambridge University Press.
7. Kirstein AF, Woolley, RM (1967) Symmetrical bending of thin circular elastic plates on equally spaced point supports. J Res. Natl. Bur. Stand. C 71.1, 1-10.

8. Staudacher M, Lube T, Supancic P (2023) The Ball-on-Three-Balls strength test for discs and plates: Extending and simplifying stress evaluation. J. Eur. Ceram. Soc. 2023, 43(2): 648-660.

9. Strobl S, Supancic P, Lube T, et al (2012) Toughness measurement on ball specimens. Part I: Theoretical analysis. J. Eur. Ceram. Soc. 32.6, 1163-1173.

10. Umeda M, Sugiyama T, Nagase F, et al (2010) Behavior of coated fuel particle of high-temperature gas-cooled reactor under reactivity-initiated accident conditions. J Nucl. Sci. Technol. 47.11, 991-997.

11. Terrani KA, Jolly BC, Harp JM (2020) Uranium nitride tristructural-isotropic fuel particle. J. Nucl. Mater. 531, 152034.

12. Supancic P, Danzer R, Harrer W, et al (2009) Strength tests on silicon nitride balls. Key Eng. Mater. 409: 193-200.

13. Xiao Y, Meng M, Daouadji A, et al (2020) Effects of particle size on crushing and deformation behaviors of rockfill materials. Geosci. Front. 11.2: 375-388.

14. Zhou B, Wei D, Ku Q, et al (2020) Study on the effect of particle morphology on single particle breakage using a combined finite-discrete element method. Comput. Geotech. 122: 103532.

15. Guo SY, Hu YG (2024) Analysis of stress transfer in rectangular patch-reinforced composites with unidirectional or bidirectional interfacial damage under tensile loading. Acta. Mech. 235.11, 6519-6568.

16. Junling H, Xuan L, Qun L (2022) Application of general regression neural network in identifying interfacial parameters under mixed-mode fracture. Acta. Mech. 233.10, 3909-3921

17. Needleman A (1990) An analysis of tensile decohesion along an

interface, J. Mech. Phys. Solids. 38.3: 289-324

18. Tvergaard V, Hutchinson JW (1992) The relation between crack growth resistance and fracture process parameters in elastic-plastic solids. J. Mech. Phys. Solids. 40.6, 1377-1397.

19. Tvergaard V, Hutchinson JW (1993) The influence of plasticity on mixed mode interface toughness. J. Mech. Phys. Solids. 41.6, 1119-1135.

20. Donadon MV, De AlmeidaSFM, Arbelo MA, et al (2009) A Three-Dimensional Ply Failure Model for Composite Structures. Int. J. Aerosp. Eng. 2009.1, 486063

21. Allix O, Ladeveze P, Corigliano A (1995) Damage analysis of interlaminar fracture specimens. Compos. Struct. 31.1, 61-74.

22. Allix O, Corigliano A (1996) Modeling and simulation of crack propagation in mixed-modes interlaminar fracture specimens. Int. J. Fract. 77, 111-140.

23. De Oliveira LA, Donadon MV (2020) Delamination analysis using cohesive zone model: A discussion on traction-separation law and mixed-mode criteria. Eng. Fract. Mech. 228, 106922.

24. Liao Y, Zhang F, Pan X, et al (2023) A comparative study on tribological behavior of Al2O3. AlN. Si3N4 and ZrO2 ceramics sliding against polycrystalline diamond ball. Wear. 530, 205067.

25. Alves MFRP, Dos SantosC, Elias CN, et al (2023) Comparison between different fracture toughness techniques in zirconia dental ceramics. J. Biomed. Mater. Res. B Appl. Biomater. 111.1, 103-116

26. Wang A, Hu P, Zhang X, et al (2017) Accurate measurement of fracture toughness in structural ceramics. J. Eur. Ceram. Soc. 37.13, 4207-4212.

27. Lin H, Yin C, Mo A (2021) Zirconia based dental biomaterials:

structure, mechanical properties, biocompatibility, surface modification, and applications as implant. Front. Dent. Med. 2: 689198.

28. Petrovic M, Ivankovic A, Murphy N (2012) The mechanical properties of polycrystalline diamond as a function of strain rate and temperature. J. Eur. Ceram. Soc. 32.12: 3021-3027.
29. Ye L (1988) Role of matrix resin in delamination onset and growth in composite laminates. Compos. Sci. Technol. 33.4, 257-277.
30. Benzeggagh ML, Kenane M (1996) Measurement of mixed-mode delamination fracture toughness of unidirectional glass/epoxy composites with mixed-mode bending apparatus. Compos. Sci. Technol. 56.4, 439-449.
31. De MaioU, Greco F, Leonetti L, et al (2019) A refined diffuse cohesive approach for the failure analysis in quasibrittle materials—part II: Application to plain and reinforced concrete structures. Fatigue Fract. Eng. Mater. Struct. 42.12, 2764-2781